

# Magnetic Levitation Haptic Augmentation for Virtual Tissue Stiffness Perception

Qianqian Tong, Zhiyong Yuan<sup>1</sup>, Xiangyun Liao<sup>1</sup>, Mianlun Zheng, Tianchen Yuan, and Jianhui Zhao<sup>1</sup>

**Abstract**—Haptic-based tissue stiffness perception is essential for palpation training system, which can provide the surgeon haptic cues for improving the diagnostic abilities. However, current haptic devices, such as Geomagic Touch, fail to provide immersive and natural haptic interaction in virtual surgery due to the inherent mechanical friction, inertia, limited workspace and flawed haptic feedback. To tackle this issue, we design a novel magnetic levitation haptic device based on electromagnetic principles to augment the tissue stiffness perception in virtual environment. Users can naturally interact with the virtual tissue by tracking the motion of magnetic stylus using stereoscopic vision so that they can accurately sense the stiffness by the magnetic stylus, which moves in the magnetic field generated by our device. We propose the idea that the effective magnetic field (EMF) is closely related to the coil attitude for the first time. To fully harness the magnetic field and flexibly generate the specific magnetic field for obtaining required haptic perception, we adopt probability clouds to describe the requirement of interactive applications and put forward an algorithm to calculate the best coil attitude. Moreover, we design a control interface circuit and present a self-adaptive fuzzy proportion integration differentiation (PID) algorithm to precisely control the coil current. We evaluate our haptic device via a series of quantitative experiments which show the high consistency of the experimental and simulated magnetic flux density, the high accuracy (0.28 mm) of real-time 3D positioning and tracking of the magnetic stylus, the low power consumption of the adjustable coil configuration, and the tissue stiffness perception accuracy improvement by 2.38 percent with the self-adaptive fuzzy PID algorithm. We conduct a user study with 22 participants, and the results suggest most of the users can clearly and immersively perceive different tissue stiffness and easily detect the tissue abnormality. Experimental results demonstrate that our magnetic levitation haptic device can provide accurate tissue stiffness perception augmentation with natural and immersive haptic interaction.

**Index Terms**—Virtual tissue stiffness perception, magnetic levitation haptic feedback, surgical simulation, effective magnetic field

## 1 INTRODUCTION

HAPTIC feedback plays a key role in realizing realistic surgical simulation in virtual environment [1], [2], [3], which is usually performed for medical training, pre-operative planning, surgical performance evaluation, etc. Many medical procedures are often preceded or accompanied by palpation [4], which is usually used to examine metastases, detect tissue abnormality, and locate anatomical landmarks such as bones, muscles and pulse. It is beneficial for performing these medical tasks by including palpations in training simulators. Besides, stiffness perception is vital for performing palpations, and tissue stiffer than surrounding could be recognized as a possible tumor [5]. Therefore, it is essential to accurately provide surgeons with tissue stiffness perception augmentation in surgical simulation systems.

Currently, there are mainly two methods for augmenting tissue stiffness perception: pseudo-haptic feedback and haptic feedback. Pseudo-haptic feedback is based on tissue stiffness maps, which are provided by rolling mechanical imaging [6], [7], [8], [9] and do not require real haptic devices. Compared with pseudo-haptic feedback, haptic feedback augments tissue stiffness perception by using a haptic device to interact with virtual environments, which is similar to the way of human perceiving information.

There have been numerous studies on tissue stiffness perception augmentation using haptic devices. The most widely used haptic device is Geomagic Touch, such as Phantom Omni. Nisky et al. [10] combined a mechanical simulator with a Phantom Premium to perform the stiffness perception in laparoscopy. Son et al. [11] utilized a Phantom as the master device to perceive soft tissue in teleoperation experiments. Ullrich et al. [4] adopted two Phantom Omni devices to implement a more realistic finger grip configuration for palpation tasks by modifying the end effector of one haptic device. However, Geomagic Touch provides haptic feedback on the operation arm through the transfer of mechanical joints. Such haptic devices suffer inherent mechanical friction and a certain amount of inertia, thus it will raise an issue if the operation arm is moved quickly [12]. Additionally, the stylus' movement of such haptic devices is limited, thus the workspace is not large enough to simulate the actual medical operation.

- Q. Tong, Z. Yuan, M. Zheng, T. Yuan, and J. Zhao are with the School of Computer, Wuhan University, Wuhan, Hubei 430072, China. E-mail: {qianqiantong, jianhui.zhao}@whu.edu.cn, yuanyzywhu@gmail.com, {mianlunz, ytcpc}@163.com.
- X. Liao is with the Shenzhen Key Laboratory of Virtual Reality and Human Interaction Technology, Shenzhen Institutes of Advanced Technology, Chinese Academy of Sciences, Shenzhen, Guangzhou 510070, China. E-mail: xyunliao@gmail.com.

Manuscript received 30 June 2017; revised 31 Oct. 2017; accepted 4 Nov. 2017. Date of publication 10 Nov. 2017; date of current version 26 Oct. 2018. (Corresponding author: Zhiyong Yuan and Xiangyun Liao.)

Recommended for acceptance by D. Schmalstieg.

For information on obtaining reprints of this article, please send e-mail to: reprints@ieee.org, and reference the Digital Object Identifier below.

Digital Object Identifier no. 10.1109/TVCG.2017.2772236

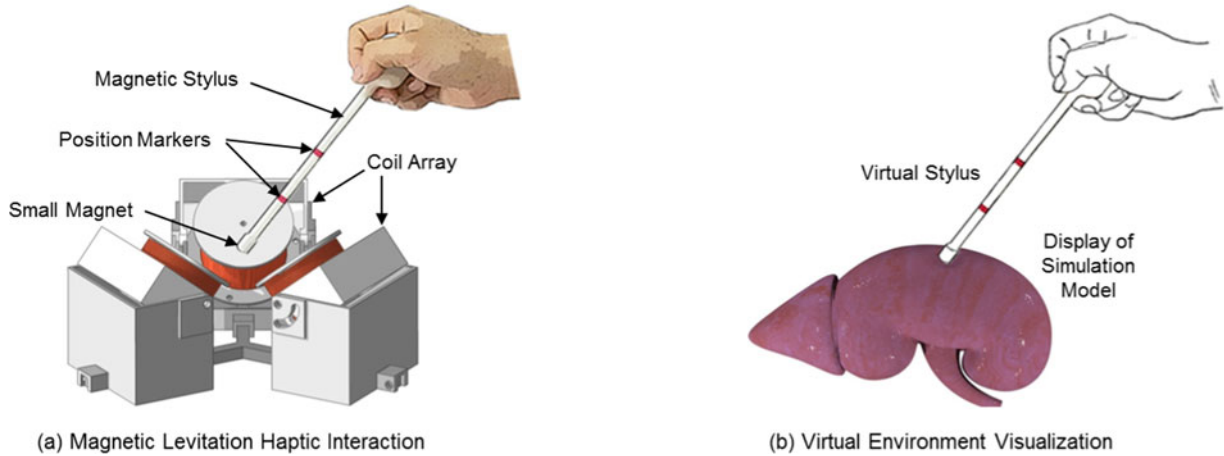


Fig. 1. Principle of the designed haptic device for augmenting the tissue stiffness perception.

Another stream of haptic devices provide haptic feedback in a contactless manner without direct skin contact, such as air-jet and ultrasonic radiation pressure [13]. The AIREAL device, designed by Disney Research [14], is an example of the air-jet haptic device, which can provide interactive haptic feedback in mid-air by stimulating the user's skin with compressed air pressure fields. However, the transfer of the air-jet method through the medium is slow and its force feedback lacks spatial and temporal qualities [15] due to the physical properties of air, making it unsuitable for the application of tissue stiffness perception. Ultrahaptics [16], designed by Carter et al., is another device to deliver mid-air haptic feedback, which employs focused ultrasound to project discrete points of haptic feedback directly to users' unadorned hands. Nevertheless, the short travelling distance, unwanted noise, and safety issues of ultrasonic method limit the applications of ultrasound-based haptic devices.

To provide haptic interaction with low static friction and low inertia, Hollis et al. [17], [18] developed a haptic device based on magnetic levitation principles, producing haptic feedback when electric currents interact with permanent magnets that fixed along the inner walls of the device. This device eliminates the mechanical friction and transfer joints, thus it has the potential to help users better perceive soft tissue [19]. However, its workspace is small because the movement of its handle is limited. Berkelman et al. [20], [21] extended the motion range by designing a planar array containing 10 cylindrical electromagnetism coils, producing haptic feedback on the planar array via a suspense stylus. Additionally, Hu et al. [22] invented a magnetic levitation haptic feedback system for open surgery simulation and training system [23]. However, Berkelman simply placed coils on a hexagonal plane [24], [25] and Hu decentralized the coils into a concave area [22], [23]. They did not concern the problem that some magnetic field areas may not provide the required feedback force. Besides, they have not yet provided a reasonable explanation about how to place the coils, that is, how to determine the suitable position and angle of coils for producing accurate haptic feedback while saving energy. Therefore, these existing haptic devices lack scalability because of the fixed coil array and lacking of the theoretical support for the design of coil array.

Inspired by the work of magnetic levitation haptic feedback [18], [21], [22], in this paper we propose a novel

magnetic levitation haptic device for providing accurate and immersive tissue stiffness perception augmentation. As shown in Fig. 1, the device is based on electromagnetic principles, and current-carrying coils generate effective magnetic field (EMF) in the workspace. Users can move our magnetic stylus (a stylus equipped with a small magnet with component of NdFe52) freely in the workspace and obtain a natural haptic feedback. The magnetic stylus is tracked using our cost-effective stereoscopic tracking module. When the interaction between the magnetic stylus and virtual soft tissue is detected, the coil array produces the corresponding EMF to generate haptic feedback. Different from the existing work [23], [26] that place the coils with no theoretical basis, we provide a reasonable explanation by simulating the EMF generated around current-carrying coils [27], present an algorithm to calculate the best coil attitude, and design an adjustable coil configuration. To avoid haptic perception affected by the external disturbance and coils' temperature rising as the conduction time increases, we present a self-adaptive fuzzy PID algorithm to control coil current accurately. The contributions of this paper are summarized as follows.

- We propose a novel magnetic levitation haptic device for augmenting tissue stiffness perception in a natural manner based on electromagnetic principles. The device has advantages of none mechanical friction, easy expansibility, high accuracy and low power consumption.
- We provide a reasonable way to design the coil array by simulating the EMF generated around current-carrying coils. Simulation results indicate that the magnetic field can be sufficiently used when the coils are placed on an appropriate attitude.
- We adopt probability clouds to describe the requirement of interactive applications and present an algorithm to calculate the best coil attitude. Consequently, the power consumption of our haptic device is low and it can be expanded to other applications conveniently.
- A self-adaptive fuzzy proportion integration differentiation (PID) algorithm is presented to stably and precisely control the coil current so as to generate accurate EMF and provide users with high precision haptic feedback.

The remaining of this paper is organized as follows. Section 2 reviews related work on tissue stiffness perception and haptic devices. Section 3 describes the design method of our magnetic levitation haptic device. Section 4 describes the experiments and results. Section 5 discusses the experimental results and conclusions are drawn in Section 6.

## 2 RELATED WORK

Surgeons often use special surgical instrument to manipulate organs or tissue in many medical procedures and their clinical skills of medical professionals strongly rely on the sense of touch [28]. It is necessary to augment tissue stiffness perception in virtual surgery training systems to improve the immersive surgical environment. Haptic devices can be used to perceive virtual object, and improve the immersive sense of interaction with the virtual environment [29].

Many reserchers have studied the haptic perception augmentation. Li et al. [8] proposed a tissue stiffness simulation technique based on tissue stiffness maps provided by rolling mechanical imaging using pseudo-haptic feedback. Disney Research [14] designed the AIREAL device, which is an example of the air-jet haptic device, providing haptic feedback in mid-air by stimulating users' skin with compressed air pressure fields. However, the transfer of the air-jet method is slow and its force feedback lacks spatial and temporal qualities [15]. Carter et al. [16] designed Ultrahaptics by employing focused ultrasound to project discrete points of haptic feedback directly to users' unadorned hands. Hoshi et al. [30] developed an interactive holographic system with haptic feedback by combining 4 ultrasound transducer arrays. Long et al. [31] applied the principles of acoustic radiation force and put forward a method for creating three-dimensional haptic shapes in mid-air using focused ultrasound. Nevertheless, the application of ultrasound-based haptic devices is limited because of its short travelling distance, unwanted noise, and safety issues.

Kesner et al. [32] developed a motion-compensated actuated catheter system that enabled users to achieve more tactile information by providing haptic feedback during palpation procedures. Quek et al. [33] designed a 1 degree of freedom (DOF) skin stretch device to augment stiffness perception. Li et al. [34] created a virtual tissue model and users can identify tumors embedded in the tissue model using a Phantom device. Ullrich and Kuhlen [4] utilized two Phantom Omni to implement bimanual interaction. One hand was used for needle insertion, and the other hand performed the palpation operation using their modified palpation pad. However, these haptic devices used for enhancing haptic perception are mechanical, which possess inherent friction because of mechanical linkages and transmissions and affect the haptic experience.

To provide haptic interaction with low inertia and low static friction, Hollis et al. [17], [35], [36] initially used Lorentz magnetic levitation to design a haptic feedback system called Magic Wrist. Subsequently, Hollis et al. [18], [37], [38] developed Butterfly Haptics' magnetic levitation haptic device. This device eliminates bulky links and general mechanical complexity of other haptic devices and it is similar to a computer mouse with six degrees of freedom. Wu et al. [19] used such Lorentz levitation haptic device for

perceptual discrimination. But the workspace of this device is limited resulting from the limited movement of its stylus.

Berkelman et al. [36], [39], [40] winded coils around the handle as a suspension. The coils cut magnetic induction lines generated by pairs of permanent magnets to realize haptic feedback when the suspension handle moves or rotates. Given the limitation of translational and rotational range of the suspension handle, Berkelman et al. [20], [21], [41] extended the motion range by designing a planar array which contains 10 cylindrical electromagnetism coils, providing force feedback for the suspense stylus on the planar array. Moreover, Berkelman et al. [24] also presented a novel system, which can generate 3D graphics and high-fidelity haptic feedback seamlessly at the same physical location. Subsequently, they increased the number of coils to 27, which can provide 6-DOF feedback force [25]. In addition, Hu et al. [22] invented a type of electromagnetism based haptic feedback system. They then designed an open surgery simulation and training system, which was preliminarily verified using a 1-DOF palpation simulation [23].

The above magnetic levitation haptic devices have advantages of no mechanical friction, possessing the potential to provide high-precision haptic feedback. We simulated the characteristic of the magnetic field generated by current-carrying coils. The simulation results show that some magnetic field areas can not provide the required feedback force and the effective magnetic field is related to coil configuration. However, researchers [23], [26] did not concern this issue and have not yet provided a reasonable explanation about how to design their coil configuration. In this paper, we study the above issues in depth, aiming at designing a novel magnetic levitation haptic device for augmenting tissue stiffness perception in a natural manner. We adopt probability clouds to describe the requirement of interactive applications and present an algorithm to calculate the best coil attitude, which can guide us to design the best coil configuration for different interactive applications. Besides, the existing magnetic levitation system usually adopted classical control algorithm with constant proportional, differential coefficients [26]. However, the coil resistance will increase as the conduction time increases, leading to the electric current of coils decreasing. We present a self-adaptive fuzzy PID algorithm to control coil current accurately.

## 3 MATERIALS AND METHODS

As shown in Fig. 2, our magnetic levitation haptic device is composed of stereoscopic tracking module, magnetic stylus, coil array, coil driver module, visualization module, etc. When the operator uses the magnetic stylus to interact with virtual soft tissue, the stereoscopic tracking module tracks the motion of the magnetic stylus in real time and sends the location information to the visualization module. The visualization module performs collision detection of tool-tissue and computes the feedback force. Then, the current of each coil is calculated using the method of [26] according to the calculated feedback force. The coil driver module intelligently adjusts the current of each coil, making the coil array generate effective magnetic field corresponding to the interactive process. Finally, the magnetic stylus receives the

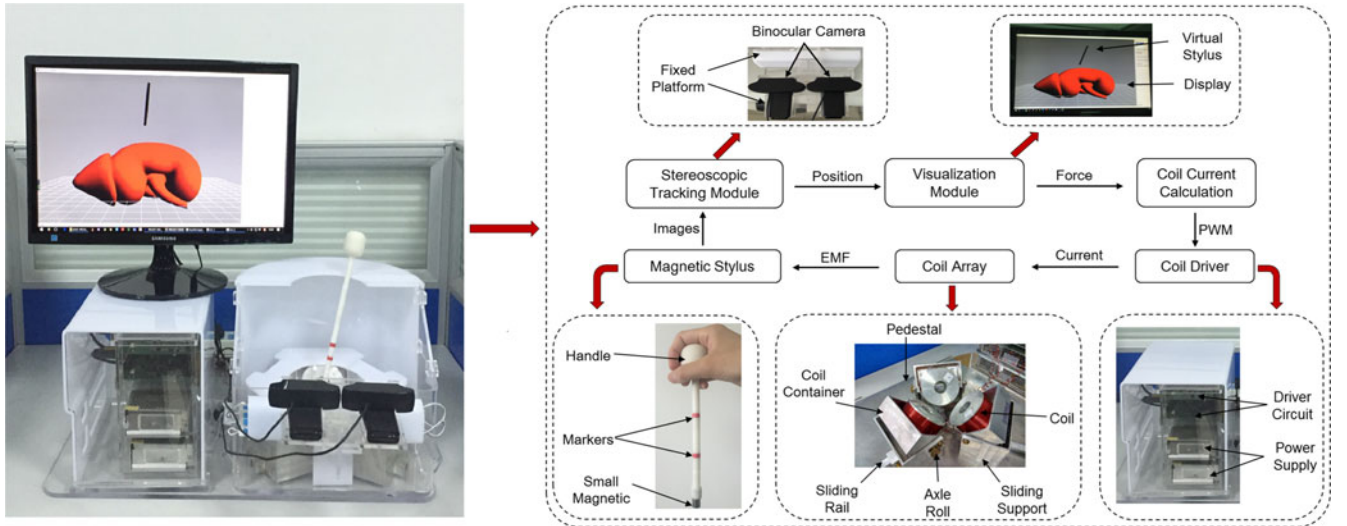


Fig. 2. The left part is our magnetic levitation haptic device and the right part depicts its overall design.

same force as the virtual stylus and transmits it to the user. Consequently, the user can distinguish soft tissue of different stiffness according to the haptic perception.

### 3.1 Real-Time Stereoscopic Navigation

Our magnetic stylus is specially designed to enable users to interact with virtual scenes freely. As depicted in Fig. 2, a small magnet is embedded at the bottom of our magnetic stylus. The magnetic stylus consists of two small rods and red markers are embedded in the connections between small rods. Precisely tracking the position and orientation of the magnetic stylus in real time is essential to accurately compute coils' current and generate the corresponding magnet field. The existing work usually used a commercial position tracking system to track the handle [24], [25], which is expensive. To develop a cost-effective tracking system with sub-millimeter accuracy for achieving highly precise haptic perception, we utilize binocular vision to navigate the interactive process due to its advantages of none contact, high accuracy, simple operation and good stability, etc. During the interactive process, two RGB cameras locate the position of the magnetic stylus by tracking red markers in real time. We perform calibration using the calibration method by Zhang [42]. In order to track the magnetic stylus in real time while ensuring sub-millimeter accuracy, we adopt coarse-to-fine [43] and parallel processing method to detect markers.

For each image frame  $I$  (the size is  $1280 \times 720$  in this paper), it is time consuming to detect red pixels line-by-line. To improve the segmentation efficiency, we first segment the region of interest  $I_{roi}$  of the image  $I$ , and  $I_{roi}$  contains all red markers. Specifically, we divide  $I$  into  $m$  regions at first, that is  $I_1, I_2, \dots, I_m$  and  $I = I_1 \cup I_2 \cup \dots \cup I_m$ . For the  $m$  regions, we adopt multi-threading processing to detect red pixels line-by-line based on the threshold method. Supposing that the region of detected red pixels of  $I_i$  is  $S_i$ , thus  $S_i \in I_i$  and  $S_i = \emptyset$  if there is no red pixel in  $I_i$ . Therefore, the region of all red pixels in image  $I$  is  $S_R$

$$S_R = S_1 \cup S_2 \cup \dots \cup S_m. \quad (1)$$

Supposing that the minimum external rectangle of  $S_R$  is  $T_1$ , and  $S_i \in T_1 (i = 1, 2, \dots, m)$ . To improve the robustness of marker detection, we add an offset  $\varepsilon$  for  $T_1$  to obtain  $T_2$  and  $T_1 \in T_2$ . Therefore, the region of interest of the image  $I$  is  $I_{roi} = I \cap T_2$ .  $S_i \in T_2 (i = 1, 2, \dots, m)$  and  $I_{roi}$  contains all red pixels. Obviously,  $I_{roi}$  is smaller than the raw image  $I$ , which helps to avoid dealing with redundant information.

Subsequently, the markers are segmented from  $I_{roi}$ . To alleviate the impact of edge blur and improve the segmentation accuracy, we blur  $I_{roi}$  adopting a Gaussian kernel smooth filter and the blurred image is  $I_{blur}$ . We progressively scan image  $I_{blur}$  and detect whether the pixel is red. When a red pixel is detected, we detect the red region using a recursion method. At the end of the recursion, we obtain the sum of the coordinates of all red pixels and the number of red pixels in the red area. The center coordinate of the region is calculated by dividing the sum of the coordinates of all red pixels using the number of red pixels. The center coordinates of all red markers can be obtained while scanning to the end of  $I_{blur}$ .

Eventually, the spatial position of red markers is calculated according to their position in the two images acquired by our RGB cameras and parameters of the cameras. The distance between markers and the distance between the markers and the tip of our magnetic stylus are known. Therefore, the position and orientation of the magnetic stylus can be calculated according to the coordinates of markers. In this paper, red markers are embedded in our magnetic stylus and the center of markers are on the center line of the stylus, which is beneficial for ensuring that the position information of the magnetic stylus calculated by the coordinates of markers is accurate.

### 3.2 Adjustable Coil Configuration

After tracking the position of the magnetic stylus, we calculate the feedback force according to our previously established interaction model. It is essential to accurately compute the current in the coils to generate the corresponding magnet field. We adopt the method of [26] to calculate the current for each coil. According to Biot-Savart Law, the magnetic field can be calculated by  $B = AI_c$ . Here  $I_c$  denotes

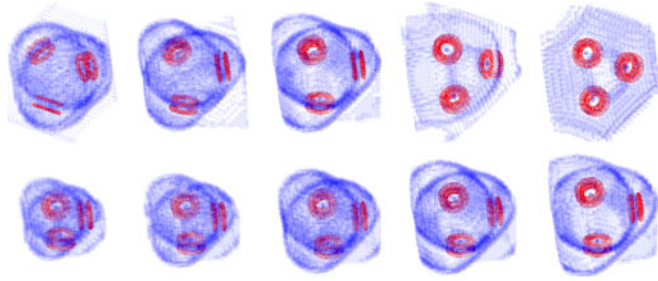


Fig. 3. The relationship between EMF and the coil attitude. The top row shows the relationship between EMF and coil angle and the bottom row shows the relationship between EMF and the distance among three coils.

the electric current value and  $\mathbf{A}$  is the current linear coefficient, which is related to the coil attitude. We adopt the method of literature [26] to confirm the linear coefficient matrix  $\mathbf{A}$ , and thus the electric current to be loaded of each coil can be solved using

$$I_c = \mathbf{A}^{-1}\mathbf{B}. \quad (2)$$

### 3.2.1 Magnetic Field Simulation

To reasonably design the coil array, we simulated the characteristic of the magnetic field generated by a current-carrying coil using Ansoft finite element analysis and Matlab software. In our magnetic levitation haptic system, three current-carrying cylindrical coils are used to produce the magnetic field. Each cylindrical coil consists of many toroidal coils and the whole cylindrical coil is considered as a superposition of multiple uniformly distributed toroidal coils. The parameters of each cylindrical coil are as follows: axial length  $H = 62$  mm; inner radius  $R_1 = 13$  mm; outer radius of coils  $R_2 = 23$  mm; number of coil turns  $N = 1041$ ; and the coil material is copper.

Equation (2) may have no theoretical solution for the reason that the determinant of matrix  $\mathbf{A}$  may be zero. In such case, the haptic device cannot provide the needed feedback force to the user. Therefore, a key process to design a magnetic levitation haptic device for haptic perception is to determine the effective magnetic field area (the determinant of matrix  $\mathbf{A}$  is not zero) adapting to the interactive application, where the current of each coil to be loaded can be resolved.

In this paper, we simulate the relationship between the EMF area and the coil attitude using finite element method (FEM). As shown in Fig. 3, the red region denotes three coils of different attitudes, the blue region shows a sphere, and the EMF area is in the interior of the sphere. The top figures show the relationship between the EMF area and the coil angle varying from 0 and 90 degrees. We can see that the EMF area gradually expands as the angle increases, whereas its position is far from the coil plane. The bottom figures depict the relationship between the EMF area and the distance between three coils. Similarly, the EMF area gradually expands with the increase of distance, and the EMF area is also increasingly far from three coils.

From the above simulation results, we can see that the EMF area is closely related to the coil attitude. If an interactive process just needs vertical magnetic field in a large area, it would be good to place coils in the vertical direction. Whereas if a magnetic field of various directions is needed

in a small area, it would be good to place the coils toward this range from different directions. Therefore, it is obvious that a better coil attitude helps to reduce coil current so as to produce a certain magnetic field.

### 3.2.2 Coil Attitude Calculation

To quantitatively calculate the best coil attitude and reduce the power consumption, we adopt probability clouds to describe the requirement of interactive applications and optimize the coil attitude by regarding the lowest power consumption as the objective function.

Supposing  $\mathbf{Q}$  is the interactive requirement of an interactive application in the time period  $T$ . We define  $\mathbf{Q}$  as a function  $\Theta$  of position and magnetic field regarded to time

$$\mathbf{Q}(t) = \Theta(\mathbf{L}(t), \mathbf{B}(t)), \quad (3)$$

where  $\mathbf{L}(t)$  and  $\mathbf{B}(t)$  are the position and magnetic field needed in the interaction process at time  $t(t \in [0, T])$ , respectively.  $\mathbf{L}(t)$  and  $\mathbf{B}(t)$  are all 3D vectors, thus Equation (3) can be denoted as

$$\mathbf{Q}(t) = \Theta(L_x(t), L_y(t), L_z(t), B_x(t), B_y(t), B_z(t)). \quad (4)$$

We denote the joint distribution function of interactive requirement as  $F(\mathbf{L}, \mathbf{B})$  (or  $F(L_x, L_y, L_z, B_x, B_y, B_z)$ ). For arbitrary position  $\mathbf{L}_i$  and magnetic field  $\mathbf{B}_i$ , we define  $F(\mathbf{L}_i, \mathbf{B}_i)$  as

$$F(\mathbf{L}_i, \mathbf{B}_i) = \frac{m(\Psi(\mathbf{L}_i, \mathbf{B}_i))}{T}, \quad (5)$$

where  $\Psi(\mathbf{L}_i, \mathbf{B}_i)$  is the assembly of the regions that satisfy the following constraints at the time period  $t \in [0, T]$ :  $L_x(t) \leq L_{ix} \cap L_y(t) \leq L_{iy} \cap L_z(t) \leq L_{iz} \cap B_x(t) \leq B_{ix} \cap B_y(t) \leq B_{iy} \cap B_z(t) \leq B_{iz}$ . The symbol “ $\cap$ ” denotes “and”.  $m(\Psi(\mathbf{L}_i, \mathbf{B}_i))$  is the measurement of  $\Psi$ , that is the time span occupying the time period  $t \in [0, T]$ .

We denote the joint probability density function of the interactive requirements as  $f(\mathbf{L}, \mathbf{B})$ . For arbitrary position  $\mathbf{L}_i$  and magnetic field  $\mathbf{B}_i$ ,  $f(\mathbf{L}, \mathbf{B})$  is defined to be

$$f(\mathbf{L}_i, \mathbf{B}_i) = \frac{\partial^6 F(\mathbf{L}_i, \mathbf{B}_i)}{\partial L_{ix} \partial L_{iy} \partial L_{iz} \partial B_{ix} \partial B_{iy} \partial B_{iz}}. \quad (6)$$

In practical application, the interaction process is usually denoted as a discrete form, Equation (6) can be written as

$$f(\mathbf{L}_i, \mathbf{B}_i) = \frac{M(\Psi(\mathbf{L}_i, \mathbf{B}_i))}{N}, \quad (7)$$

where  $N$  is the total length of the discrete sequence,  $M(\Psi(\mathbf{L}_i, \mathbf{B}_i))$  the number of  $\Psi(\mathbf{L}_i, \mathbf{B}_i)$  in the sequence. The joint probability density function  $f(\mathbf{L}, \mathbf{B})$  in 6D space describes the possibility in which a particular magnetic field is needed at a particular position in the interactive process. We adopt the possibility clouds  $f(\mathbf{L}, \mathbf{B})$  to describe the requirements of interactive applications in this paper.

For a particular interactive requirement, we calculate the best coil attitude by using the aforementioned possibility clouds. We define an optimization evaluation function  $E$  as

$$E = \iint_{L, B} f(\mathbf{L}, \mathbf{B}) \mathbf{B}^T \mathbf{A}^{-1}(\mathbf{L})^T \mathbf{A}^{-1}(\mathbf{L}) \mathbf{B} d(\mathbf{L}, \mathbf{B}), \quad (8)$$

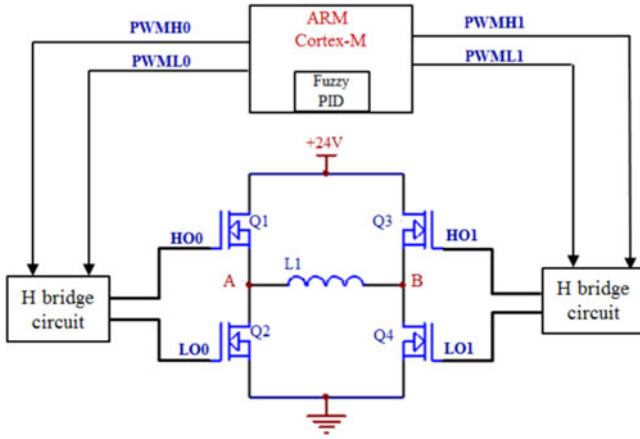


Fig. 4. Coil driver circuit based on complementary PWM driving mode.

where  $E$  denotes the power consumption of coils in the interactive process, and  $\mathbf{A}(\mathbf{L})$  is three-coil coefficient matrix in position  $\mathbf{L}$ .  $d(\mathbf{L}, \mathbf{B})$  is the integral element of space  $(\mathbf{L}, \mathbf{B})$ .

In the circumstance that the three coils are symmetrical, there are formulae  $\varphi = \alpha = \beta = \gamma$ ,  $l = l_A = l_B = l_C$ .  $\alpha, \beta, \gamma$  are the placement angles of the three coils and  $l_A, l_B, l_C$  are the distances between the coils and center axis. The best coil attitude is the position where power consumption  $E$  is the minimum in space  $(\varphi, l)$ . Algorithm 1 describes the algorithm of calculating the best coil attitude.

---

#### Algorithm 1. Coil Attitude Calculation

---

- 1: Initialize the minimum optimization evaluation function  $E_{\min} = \infty$ .
  - 2: **while**  $(\varphi, l)$  in the search area **do**
  - 3: initialize the evaluation function,  $E = 0$ ;
  - 4: **for** each  $(L_i, B_i)$  in the requirement sequence **do**
  - 5: Calculate the coefficient matrix  $\mathbf{A}(\mathbf{L})$  at position  $\mathbf{L}_i$ , and its inverse matrix  $\mathbf{A}^{-1}(\mathbf{L})$ ;
  - 6: Calculate the power consumption  $\mathbf{B}^T \mathbf{A}^{-1}(\mathbf{L})^T \mathbf{A}^{-1}(\mathbf{L}) \mathbf{B}$  at position  $\mathbf{L}_i$ ;
  - 7: Accumulate the power consumption  $E = E + \mathbf{B}^T \mathbf{A}^{-1}(\mathbf{L})^T \mathbf{A}^{-1}(\mathbf{L}) \mathbf{B}$ ;
  - 8: **if**  $E_{\min} > E$  **then**
  - 9:  $E_{\min} = E$ , record the current  $(\varphi, l)$ ;
  - 10: **end if**
  - 11: **end for**
  - 12: Get the  $(\varphi, l)$  and optimize the  $E$ ;
  - 13: **end while**
- 

### 3.2.3 Adjustable Coil Array

To adjust the coil attitude conveniently, we design a special mechanical configuration for the coil array. As shown in Fig. 2, we design a pedestal to adjust the attitude of the three coils, which contains three sliding supports, three coil containers and three coils. The sliding rails are placed on the pedestal, the sliding supports are placed 120 degree apart on the sliding rails, the coil containers are placed on the sliding supports, and the coils are placed on the containers. Three containers are parallel to the sliding rails and the position of three coils can be adjusted by controlling the position of three containers on the sliding rails. Moreover, the angle of three coils can be freely controlled by adjusting

the axle rolls. Consequently, we can obtain the best coil attitude for different virtual reality applications of perceiving the tissue stiffness by adjusting the coil attitude.

## 3.3 Coil Driver

### 3.3.1 Coil Driver Circuit

We design a coil driver circuit to control the coil current. As shown in Fig. 4, the ARM Cortex-M MCU is the core controller which generates a pulse width modulation (PWM) signal to drive the H bridge circuit. The H bridge circuit adopts the PWM signal to control the state (conduction or cutoff) of the metal-oxide-semiconductor field-effect transistors (MOSFETs) on the arms of the H bridge circuit so as to achieve a variation in the current direction of coils. We choose the complementary PWM driving mode to control the coil current. In Fig. 4, Q1, Q2, Q3 and Q4 are all NMOSFETs (NMOSS). Q1 and Q2 compose a group of NMOSSs, which alternately conduct on the same side of the H-bridge, and Q3 and Q4 are another group. If Q1 and Q4 conduct at the same time, two ends A and B of the coil will be forward voltage and it will be backward voltage when Q2 and Q3 conduct. We use two H-bridge driver chips to realize full-bridge driving. For a half-bridge, the PWM signals of two channels are sent to an AND gate chip, and its output is used to protect the NMOSSs. The current of the coil can be controlled by adjusting the duty ratio of the two PWM signals, thus to generate the required magnetic field.

### 3.3.2 Coil Current Control

Usually, there would be a certain deviation between the actual coil current and the needed current in an interactive process. Additionally, as the conduction time increases, the coil resistance will increase, resulting in feedback force diminishing and users feeling the tissue as softer. We propose a self-adaptive fuzzy PID algorithm to resolve this issue.

PID algorithm does proportional, integral and differential operations according to the error signal. The sum of the three operation results is the output of the controlled signal. The mathematical model of PID algorithm is denoted as

$$u(t) = K_p \left[ e(t) + \frac{1}{T_i} \int_0^t e(t) dt + T_d \frac{de(t)}{dt} \right], \quad (9)$$

where  $u(t)$  is the output control variable of PID,  $K_p$  is a proportionality coefficient,  $T_i$  is integral time constant,  $T_d$  is differential time constant, and  $e(t)$  is the error signal. Note the sampling period as  $T$ , thus the integral coefficient of PID is  $K_i = K_p \frac{T}{T_i}$  and the differential coefficient is  $K_d = K_p \frac{T}{T_d}$ .

According to Equation (9), the differential equation of PID algorithm for coil current control is

$$u(k) = K_p e(k) + K_i \sum_{n=0}^k e(n) + K_d [e(k) - e(k-1)], \quad (10)$$

where  $u(k)$  is the adjusted coil current at time  $k$ ,  $e(k)$  is the deviation between needed current  $r(k)$  and actual current  $c(k)$ , that is  $e(k) = r(k) - c(k)$  and  $e_c(k)$  is the variation rate of  $e(k)$ .  $K_p, K_i, K_d$  are proportional, integral and differential coefficients of PID respectively and  $\Delta k_p, \Delta k_i, \Delta k_d$  are their correction values. In this paper, we use a current sensor to

detect the current of the sampling resistor, which is in series with the coil. The detected current is the actual current  $c(k)$  of coils. According to Equation (10)

$$\Delta u(k) = K_p(e(k) - e(k-1)) + K_i e(k) + K_d(e(k) - 2e(k-1) + e(k-2)), \quad (11)$$

where  $\Delta u(k)$  is the coil current increment calculated by PID algorithm at time  $k$ .

The difficulty of the classical PID algorithm lies in the parameter self-tuning in the proportional, integral and differential link. For general accuracy requirements, the patchwork approach can be used. To improve the performance of our haptic device and ensure accurate stiffness perception, we adopt the idea of fuzzy reasoning. The on-line self-tuning of  $K_p$ ,  $K_i$ , and  $K_d$  are performed according to different current deviations  $e(k)$  and variation rates  $e_c(k)$ . The key to design a fuzzy PID controller is creating a suitable fuzzy rule table. Our fuzzy rules are developed according to the current deviation  $e$  and deviation variation rate  $e_c$  of coil current. When  $|e|$  is bigger, we should take a larger  $K_p$  to speed up the system response, and take a smaller  $K_d$  to avoid differential saturation, and limit the role of integration to avoid overshoot. When  $|e|$  and  $|e_c|$  is medium,  $K_p$  should be smaller and  $K_d$  and  $K_i$  should be moderate. When  $|e|$  is smaller, that is the actual current  $c(k)$  is close to the needed current  $r(k)$ ,  $K_p$  and  $K_i$  should be increased and  $K_d$  can be bigger if  $|e_c|$  is small, otherwise,  $K_d$  can be smaller.

Supposing that  $\Delta k_p$ ,  $\Delta k_i$ , and  $\Delta k_d$  are the correction values of  $K_p$ ,  $K_i$ , and  $K_d$ , respectively. First, the deviation  $e$ , deviation variation rate  $e_c$  as well as the outputs  $\Delta k_p$ ,  $\Delta k_i$ , and  $\Delta k_d$  are fuzzed using a triangular membership function, denoting the fuzzy linguistic variables of  $e$ ,  $e_c$  as  $E$ ,  $E_c$ . The fuzzy output is then calculated by solving the fuzzy relational equation using a fuzzy reasoning of taking small operation according to our designed fuzzy rules. Then, the precise value is calculated using the weighted average method to acquire the actual outputs of  $\Delta k_p$ ,  $\Delta k_i$ , and  $\Delta k_d$  after the scale transformation. Finally, we obtain the PID parameters  $K_p$ ,  $K_i$ , and  $K_d$ , which are used to calculate the incremental value of the PWM signal. Consequently, the ARM Cortex-M MCU accomplishes control of the coil current in real time. Algorithm 2 describes the intelligent control algorithm for coil current.

## 4 EXPERIMENTS

To evaluate the performance of our magnetic levitation haptic device, we conducted quantitative and qualitative experiments. In the quantitative experiment, we first compared the experimental and simulation data of magnetic flux density generated by a single coil as well as three coils. Next, we designed a calibration platform and evaluated the accuracy of our stereoscopic tracking module. Subsequently, we analyzed the effectiveness of our designed adjustable coil array. Finally, the performance of the presented self-adaptive fuzzy PID algorithm was verified. In the qualitative experiment, the designed device was subjectively compared with the Phantom Omni device by recruiting participants to distinguish objects of different stiffness, detect tissue abnormality and complete a questionnaire.

TABLE 1  
Comparison between the Experimental and Simulation Data of Magnetic Flux Density for a Single Coil

Distance (mm)	Experimental data (mT)				Simulation data (mT)			
	0.5	1.0	1.5	2.0	0.5	1.0	1.5	2.0
69	15	28.8	40	53.2	13	26.3	39	52.1
74	9.4	18	26.6	35.6	8.26	16.6	25	32.7
79	6.1	11.8	17.5	21.2	5.47	11.1	16	22.1
84	4.1	7.8	11.9	14.2	3.64	7.56	11	14.4
89	2.6	5.1	7.7	9.9	2.7	5.3	8.0	10.8
94	2.0	4.0	5.8	7.1	2.03	4.07	6.0	7.96
99	1.5	2.9	4.4	5.3	1.54	3.12	4.6	6.18
104	1.1	2.2	3.3	3.9	1.14	2.29	3.5	4.67
109	0.9	1.7	2.4	3.1	0.99	1.20	3.0	3.99
114	0.7	1.4	1.9	2.5	0.81	1.65	2.5	3.28
119	0.5	1.1	1.6	1.9	0.69	1.38	2.1	2.74
124	0.4	0.9	1.4	1.7	0.56	1.12	1.67	2.28

### Algorithm 2. Self-Adaptive Fuzzy PID for Coil Current Control

- 1: Initialize system configuration, such as the PWM controller, timer, etc.; Initialize the needed current flag flag1, the actual coil current flag flag2, and coil current update flag flag3 as 0; Initialize PID parameters  $K_{p0}$ ,  $K_{i0}$ ,  $K_{d0}$ .
- 2: **while** 1 **do**
- 3:   **if** flag1==1 (set by interruption) **then**
- 4:     Digitize the needed current  $r$ , flag1=0;
- 5:   **end if**
- 6:   **if** flag2==1 (set by interruption) **then**
- 7:     Obtain the actual coil current  $c$ , flag2=0, flag3=1;
- 8:   **end if**
- 9:   **if** flag3==1 **then**
- 10:     Calculate the error  $e$  and its change rate  $e_c$ ;
- 11:     Fuzz  $e$ ,  $e_c$  and the fuzzy output  $\Delta k_p$ ,  $\Delta k_i$ ,  $\Delta k_d$  using a triangular membership function;
- 12:     Query fuzzy rule table, calculate the fuzzy output;
- 13:     Calculate the precise value of the fuzzy output using weighted average method, and acquire actual  $\Delta k_p$ ,  $\Delta k_i$ ,  $\Delta k_d$  by scale transformation;
- 14:     Adjust  $K_{p0}$ ,  $K_{i0}$ ,  $K_{d0}$  using  $\Delta k_p$ ,  $\Delta k_i$ ,  $\Delta k_d$ ;
- 15:     Calculate the output signal  $pwm_{out}$ ;
- 16:     Limit  $pwm_{out}$  according to the set threshold;
- 17:   **end if**
- 18: **end while**

## 4.1 Quantitative Experiment

### 4.1.1 Comparison of Experimental and Simulation Data of Magnetic Flux Density

We performed two groups of comparative experiments for the experimental and simulation data of a single coil. One is the relationship between the magnetic flux density and the position when the coil current is steady. The other is the relationship between the magnetic field distribution and the current. The magnetic field of a certain continuous position of the  $z$  axis was measured from (0, 0, 69) to (0, 0, 124) with a step size of 5 mm at 0.5 A, 1 A, 1.5 A and 2 A. Table 1 shows the experimental and simulation data for a single coil. The magnetic flux density of three-coil is measured at 1A and 2A in different positions on the coil center axis (from (0, 0, 80) to (0, 0, 130) with the step of 5 mm). Table 2 shows the

TABLE 2  
Comparison between the Experimental and Simulation  
Data of Magnetic Flux Density for Three-Coil

Distance (mm)	Experimental data (mT)		Simulation data (mT)	
	1.0	2.0	1.0	2.0
80	2.29	4.57	2	4.2
85	2.44	4.9	2.2	4.7
90	2.36	4.75	2.4	4.6
95	2.33	4.63	2.4	4.6
100	2.19	4.37	2.3	4.5
105	2.11	4.22	2.2	4.3
110	1.97	3.92	2.1	4.0
115	1.81	3.61	1.9	3.5
120	1.66	3.33	1.7	3.2
125	1.53	3.06	1.6	3.0
130	1.4	2.8	1.4	2.7

experimental and simulation data of magnetic flux density on the coil center axis, and the three coils are placed according to the configuration of Section 3.2.3.

As shown in Fig. 5, the horizontal coordinate represents the position of the central axis, and the vertical coordinate represents the magnetic flux density in space. It is apparent that the simulation data and the experimental data are significantly consistent. The curve of Fig. 5a depicts the magnetic flux density of a single coil, which first significantly decreases and then slows down after a certain critical value with an increasing distance. The curve in Fig. 5b shows the variation trend of the magnetic flux density of three-coil with the increasing of distance. When the coil current keeps the same, the experimental and simulation data are consistent and the magnetic field increases to a certain peak value and then decreases gradually as the distance increases. Besides, Fig. 5 demonstrates that the magnetic flux density doubles as the coil current doubles.

#### 4.1.2 Performance of Real-Time Stereoscopic Navigation

We designed a calibration platform to evaluate the positioning accuracy of our stereoscopic tracking module, as shown in the left of Fig. 6. The calibration platform was designed according to the workspace of our magnetic levitation haptic device to ensure that the visual test environment is the same

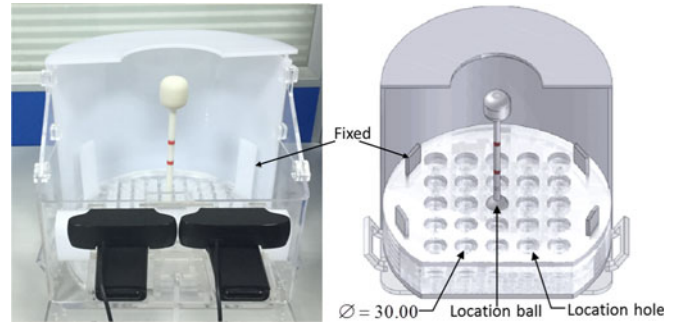


Fig. 6. The designed calibration platform for evaluating the positioning accuracy of our stereoscopic tracking module.

as its usage environment. We adopted Autodesk Inventor to design the platform with fabrication precision of 0.1 mm.

As shown in the right of Fig. 6, the calibration platform comprised 25 cylindrical location holes ( $\varnothing 30$  mm) uniformly spaced on a planar grid. Cylindrical location holes were designed to fix the tip of the stylus. Specially, we designed a spherical tip (called location ball) for the stylus, which can be just placed in the cylindrical location hole. This design is used to ensure that the tip of the stylus is fixed at a certain position. Moreover, the spherical tip can be rotated freely in the location hole so that the stylus can be placed in different poses when its tip is placed in a location hole.

To evaluate the positioning accuracy, many positioning trials (eight trails in this test) were conducted for each cylindrical location hole with different directions of the stylus for each trial. As the red markers on the stylus appeared in the field-of-view of the cameras, the position information (the orientation and the 3D coordinates of the location ball) of the stylus can be calculated in real time using our positioning method. It is worth noting that, the acquired 3D coordinates are the position information of the center of the location ball.

First, we computed the 3D coordinates of the location ball for all cylindrical location holes. For each cylindrical location hole, we analyzed the coordinate of each dimension ( $x, y, z$ ) for multiple positioning trails by computing their standard deviation ( $\sigma$ ). Besides, we computed the standard deviation of 3D position ( $\sigma_D$ ) by calculating the distance between two positioning trails. Table 3 shows the analysis results for 25 cylindrical location holes. The mean value of standard deviation for 25 cylindrical location holes is shown in the "Mean" row of Table 3. The mean value of standard

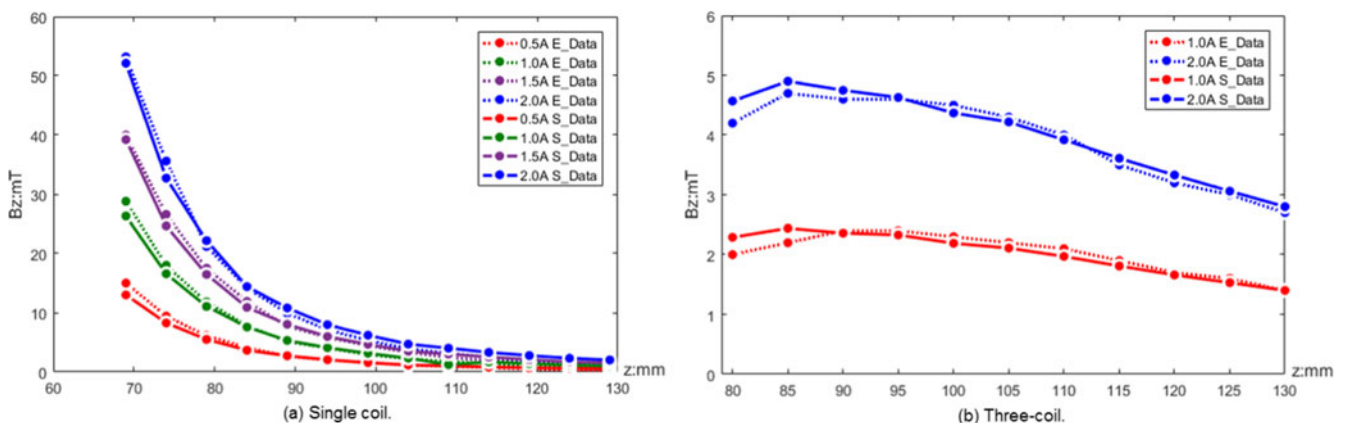


Fig. 5. Comparison chart between the experimental and simulation data of magnetic flux density for a single coil (a) and three-coil (b).

TABLE 3  
Performance of our Stereoscopic Tracking Module

Hole	$\sigma_x$ (mm)	$\sigma_y$ (mm)	$\sigma_z$ (mm)	$\sigma_D$ (mm)	Hole	$\sigma_x$ (mm)	$\sigma_y$ (mm)	$\sigma_z$ (mm)	$\sigma_D$ (mm)
1	0.56	0.37	0.31	0.31	14	0.57	0.65	0.37	0.41
2	0.40	0.20	0.39	0.25	15	0.50	0.57	0.33	0.32
3	0.34	0.39	0.36	0.23	16	0.64	0.16	0.41	0.38
4	0.40	0.46	0.54	0.35	17	0.70	0.37	0.42	0.39
5	0.50	0.55	0.45	0.26	18	0.35	0.39	0.53	0.23
6	0.40	0.28	0.56	0.29	19	0.40	0.29	0.42	0.21
7	0.40	0.12	0.34	0.18	20	0.38	0.48	0.41	0.17
8	0.58	0.33	0.41	0.35	21	0.51	0.30	0.44	0.24
9	0.66	0.58	0.50	0.36	22	0.46	0.32	0.41	0.21
10	0.50	0.57	0.51	0.43	23	0.47	0.47	0.32	0.32
11	0.50	0.23	0.39	0.20	24	0.51	0.27	0.55	0.24
12	0.53	0.43	0.36	0.30	25	0.20	0.27	0.14	0.16
13	0.54	0.44	0.31	0.22	<b>Mean</b>	0.48	0.38	0.41	0.28

Positioning errors ( $\sigma$ ) of 3D coordinates for 25 location holes.

deviation for 3D position is 0.28 mm, which demonstrates high accuracy of our stereoscopic tracking module.

When we detect red markers on the whole image (the resolution is  $1280 \times 720$ ) using a recursion method and parallel processing, the positioning speed can reach about 40 Hz. In this paper, we divide the whole image into many regions and detect red pixels of each region using the parallel processing and multi-threading processing technology. Consequently, our stereoscopic tracking module can reach 200 Hz while ensuring 3D positioning accuracy of 0.28 mm.

#### 4.1.3 Results of Coil Attitude Calculation

To assess the effectiveness of our adjustable coil array, we designed two different interaction application requirements. The first one is the interaction application of a

stylus and an elastic circular plane. The other one is the interaction application of a stylus and an elastic hemisphere. As shown in Fig. 7, the left of Fig. 7a shows the interactive requirements of the elastic circular plane, and the left of Fig. 7b shows the interactive requirements of the elastic hemisphere. Using the constraints of  $(\varphi \in [0^\circ, 90^\circ], l > \frac{2}{\sqrt{3}}R_2)$ , we calculated out the best coil attitudes for both interactive requirements adopting the algorithm presented in Section 3.2.2. The result of the elastic circular plane is  $(\varphi_0, l_0) = (90^\circ, 43.3)$ , and the result of the elastic hemisphere is  $(\varphi_0, l_0) = (80.4^\circ, 42)$ . We can see that the best coil angle for the elastic circular plane is vertical, which is similar to Berkelman [24], [25]. The best coil angle for the elastic hemisphere towards the interaction area, which is completely consistent with our simulation results described in Section 3.2.1.

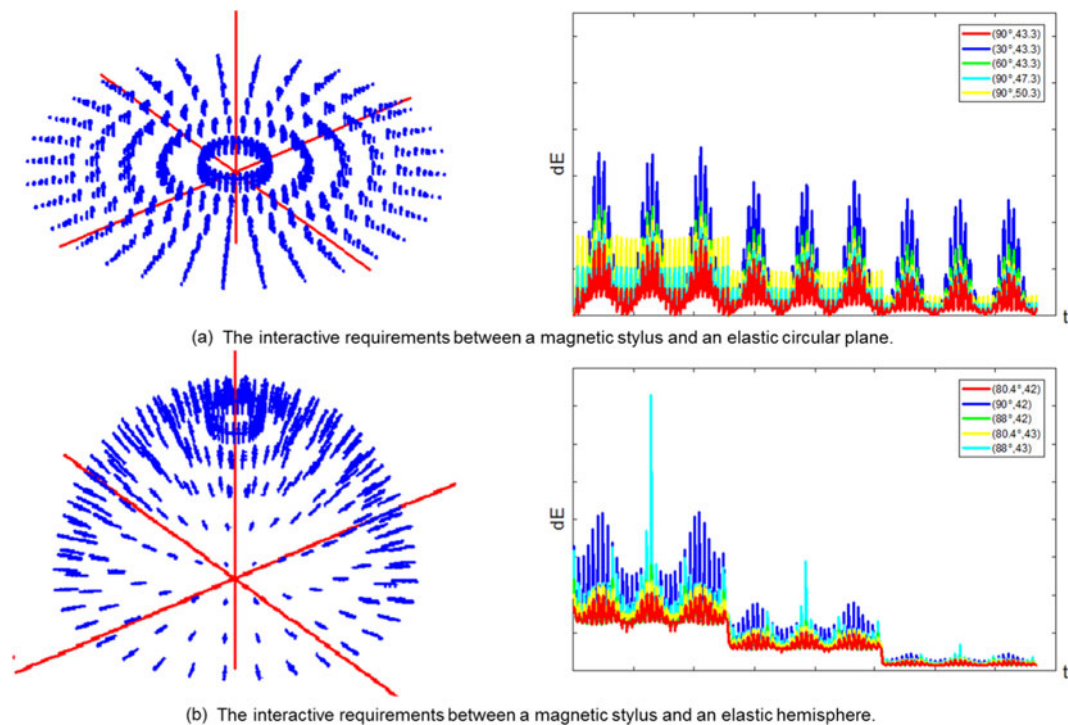


Fig. 7. Performance of our coil attitude calculation algorithm. For figure (a) and (b), the right part denotes the corresponding interactive requirement and the right denotes comparison results of different coil attitudes.

TABLE 4  
Comparison between Our Self-Adaptive Fuzzy PID Algorithm and the Classical PID Algorithm for Coil Current Control

Current (mA)	Our method			Classical PID		
	$e_m$ (mA)	$e_s$ (mA)	$e_r$ (%)	$e_m$ (mA)	$e_s$ (mA)	$e_r$ (%)
300	8.00	9.31	9.33	14.00	16.93	23.67
600	8.60	9.83	6.00	10.94	14.70	8.17
900	6.32	8.33	4.33	11.36	14.45	5.44
1,200	1.10	2.99	2.25	6.59	8.44	4.08
1,500	2.21	1.86	1.67	1.40	2.43	2.27
1,800	3.03	0.95	0.67	9.24	11.79	2.89
2,100	6.26	8.36	1.90	11.89	11.12	2.38
2,400	6.04	8.10	1.25	8.04	10.09	1.58
2,700	4.90	6.04	0.81	13.42	16.15	1.59
3,000	4.14	4.94	1.27	19.31	20.27	1.20

We compared the calculated best attitude for the elastic circular plane (the left of Fig. 7a) with two other coil attitudes which are similar to that of Berkelman [24], [25] and two other similar to that of Hu [22], [23]. The right of Fig. 7a shows their comparison results of power consumption. Its horizontal axis denotes the whole interactive process and the vertical axis is the power consumption of one interactive operation. Thus the area between the line and the horizontal axis is the total power consumption. The red line denotes our coil attitude  $(\varphi_0, l_0) = (90^\circ, 43.3)$ , and the blue line and green line denote two coil attitudes similar to Berkelman [24], [25], which are  $(\varphi_0, l_0) = (90^\circ, 47.3)$  and  $(\varphi_0, l_0) = (90^\circ, 50.3)$ , respectively. Apparently, the red line is lower than the blue line and green line. Moreover, the yellow line and cyan line denote two coil attitudes similar to Hu's method [22], [23]. The power consumption of these two coil attitudes is also higher than ours.

Additionally, we compared the calculated best attitude for the elastic hemisphere with the coil attitude employed by Berkelman [24], [25] and three other coil attitudes similar to Hu's method [22], [23]. The right of Fig. 7b shows the comparison results of power consumption. The red line denotes our coil attitude  $(\varphi_0, l_0) = (80.4^\circ, 42)$ , and the blue line denotes Berkelman's coil attitude  $(\varphi, l) = (90^\circ, 42)$ . The red line is lower than other four lines, which also demonstrates that the coil attitude calculated by our algorithm can effectively reduce coil power consumption.

#### 4.1.4 Performance of Self-Adaptive Fuzzy PID Algorithm

To evaluate the performance of the proposed self-adaptive fuzzy PID algorithm, we first compared our method with the classical PID algorithm. In the experiment, we adjusted different currents using these two methods (the current range is 300-3,000 mA, and the step is 300 mA). For each current, we analyzed the mean error ( $e_m$ ), standard deviation ( $e_s$ ) and the maximum relative error ( $e_r$ ) of 1,000 adjusted samples. The comparison results are shown in Table 4. It can be observed that the mean error, standard deviation and maximum relative error of our algorithm are all smaller than the classical PID algorithm. Specially, the mean value of the maximum relative error of our algorithm is 2.95 percent, reducing by 2.38 percent compared with the classical PID algorithm which achieves 5.33 percent. The parameters of the classical PID algorithm are  $K_p = 0.2$ ,  $K_i = 0.5$ , and  $K_d = 0.1$ , which are used as initial parameters of our algorithm.

The stability and smoothness of the magnetic field is significantly important for providing highly immersive haptic perception. We then evaluated the performance of our self-adaptive fuzzy PID algorithm for controlling continuously changing current and compared the actual magnitude of the magnetic flux density with the experimental magnitude of the magnetic flux density  $B$ . The blue line of Fig. 8a depicts the actual magnitude of the magnetic flux density. The blue solid line, red solid line and green solid line of Fig. 8b denote the calculated current of three coils adopting the method of [26]. The blue dotted line, red dotted line and green dotted line of Fig. 8b denote their corresponding controlled results using the proposed fuzzy PID algorithm, respectively. The horizontal axis of Fig. 8 denotes the whole interactive process and the value (current and magnetic of  $B$ ) of vertical axis changes with time during the interactive process. We can see that the controlled current is consistent with the calculated current. The red line of Fig. 8a depicts the magnitude of  $B$  generated by the controlled current, and it is close to the actual magnitude of  $B$ . Therefore, our haptic device can provide highly immersive haptic perception.

#### 4.2 Qualitative Experiment

Two qualitative experiments were conducted to evaluate the performance of our magnetic levitation haptic device on augmenting the tissue stiffness perception. Experiment 1 is

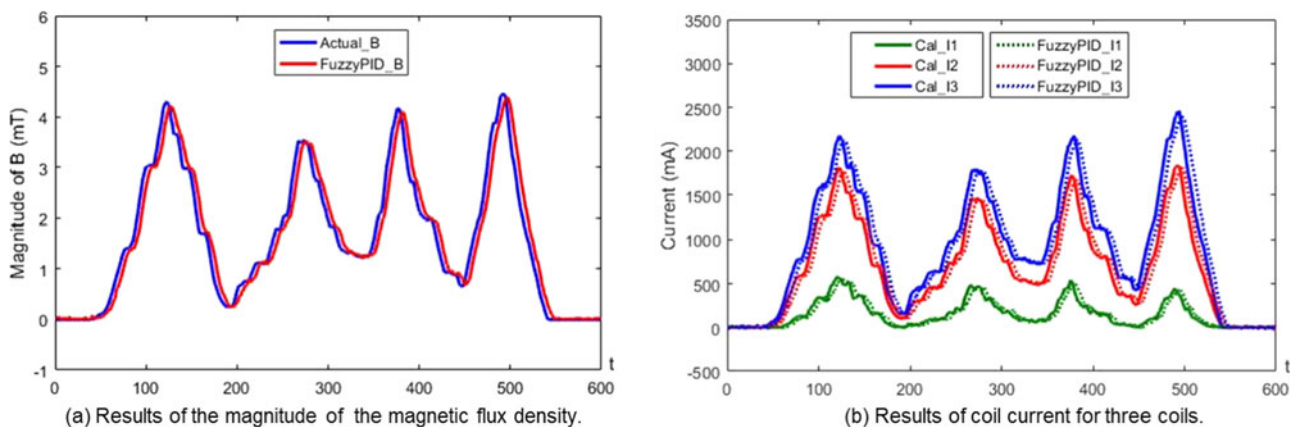


Fig. 8. Performance of our self-adaptive fuzzy PID algorithm for controlling continuously changing current.

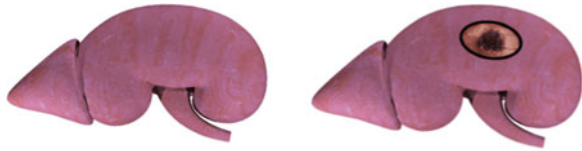


Fig. 9. Kidney model. The left is the normal tissue and the right is the abnormal tissue embedded with a lump.

used to evaluate the reliability of our haptic device to distinguish objects of different stiffness. Experiment 2 is used to evaluate the accuracy of detecting tissue abnormality.

#### 4.2.1 Participants

We recruited 22 participants (9 females and 13 males; with a mean age of 28 years old) among students and teachers. To ensure the objectivity of the experiments, nineteen participants had no previous experience with our magnetic haptic device. All of the participants did not know the goal and design of the experiments.

#### 4.2.2 Apparatus

The test hardware is our magnetic levitation haptic prototype device described in Section 3. Three coils of the device are placed 120 degree apart. The angle between each coil and the horizontal plane is 60 degree, and the distance between two coils is 40 mm. Phantom Omni is used to compare with our device for the tissue stiffness perception. The tasks of calculating our simulation model, solving the coil current and tracking the magnetic stylus are performed on a PC (Intel Xeon CPU E3-1230 V2 @ 3.30 GHz, 8.00 GB of memory).

#### 4.2.3 Design

In Experiment 1, we designed six levels of stiffness for the kidney model from small to large: A, B, C, D, E, and F. The appearances of all six objects are identical. Objects A, C, and E are first used to familiarize the participants with our haptic device and to train them to experience the process of tissue stiffness perception. Next, we disrupt the orders of A, C, E and B, D, F respectively, and the participants are asked to sort the objects according to their perception experience by using the designed haptic device and the Phantom Omni.

As shown in Fig. 9, we embedded a lump in a kidney as the abnormal tissue, and the other kidney is the normal tissue in Experiment 2.

We model the real-time deformation of kidney using Vega, which is a nonlinear FEM deformable object simulator exploited by Sin et al. [44]. The parameters of our model are as follows: the number of vertices is 16,680; the number of elements is 8,466; the simulation frame rate is 60 Hz.

#### 4.2.4 Procedure

Participants individually entered the laboratory, and they had no communication with each other. Two experiments are divided into two stages. After all participants completed the first experiment, we counted and analyzed the experimental results. If more than 80 percent of the participants can accurately distinguish the tissue of different stiffness, we continued to conduct the second experiment.

The participant read and signed an informed consent sheet after entering the laboratory. It is widely known that

TABLE 5  
QoE Questionnaire

Factor	Question
Sensory	How much did the haptic device contribute to augmenting the stiffness perception of tissue? Whether the interaction way is consistent with your habits of the real world?
Realism	How much did the perceived experiences seem consistent with your real-world experiences?
Comfort	How comfortable was the haptic device?
Satisfaction	How much did you prefer to use the device?

Each question is rated on a 5-point scale from 1 (Not at all) to 5 (Totally).

there may be sickness phenomenon in the experience of AR and VR. We told each participant he or she could interrupt the experiment at any time if encountering problems. Participants attempted to use our device according to our guidelines. After the preparatory work was completed, the participant conducted the training task. During the training task, objects A, C, and E were sorted from small to large according to the stiffness. The goal of the training task is to let the participant experience objects of different stiffness.

We conducted the first test of Experiment 1 after the training task was completed. The participant was asked to sort the objects A, C, and E, whose order was shuffled. We counted the results and then conducted the second test of Experiment 1. The participant perceived objects B, D, and F and sorted them, and the results were counted. The participant had no interaction with objects B, D, and F using our haptic device before the test, ensuring the credibility of our experiment. The participant would then rest and wait in a separate waiting area after finishing Experiment 1.

In Experiment 2, each participant was told to detect whether the kidney model contained lesions in the virtual environment. All participants were aware that the stiffness of diseased tissue is higher than that of surrounding normal tissue [5]. We told the participants that each kidney may be in one of three conditions: (1) Neither contains tissue abnormality; (2) Only one contains tissue abnormality; (3) Both contain tissue abnormality.

#### 4.2.5 Measurement of QoE: Questionnaire

After finishing experiment 2, each participant was asked to fill in a questionnaire, which is designed to evaluate the user's perceived quality of experience (QoE) for tissue stiffness perception. QoE is related to the subjective user experience with a service or an application [45]. As shown in Table 5, our questionnaire is based on four factors [46], [47]: Sensory, Realism, Comfort and Satisfaction. "Sensory" characterizes how much the haptic device contributed to augmenting the stiffness perception of tissue and whether the interaction way is consistent with user's habits of the real world. "Realism" describes how much the virtual environment is realistic. "Comfort" measures how comfortable the haptic device is to use. "Satisfaction" determines whether the user prefers to use the device. Each factor was evaluated by questions rated on a 5-point scale. The mean value was calculated for each factor, and QoE was computed as the sum of these 4 factors.

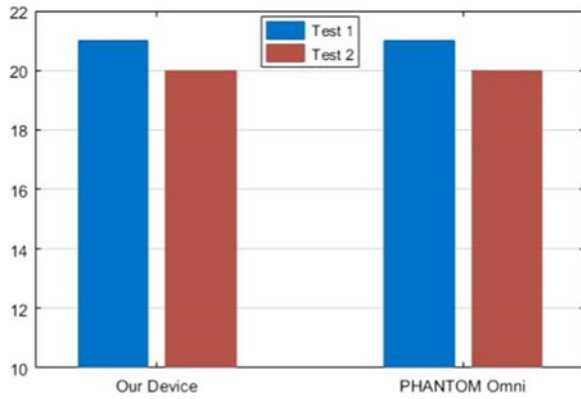


Fig. 10. Number of participants to accurately distinguish corresponding objects using the designed device and Phantom Omni.

#### 4.2.6 Results

In Experiment 1, the participants distinguished the kidney models of different stiffness. The statistical results of test 1 and test 2 using our device and Phantom Omni are shown in Fig. 10. 21 participants (95 percent) successfully distinguished the objects of different stiffness in test 1. In test 2, two participants wrongly sorted the two models of smaller stiffness (objects B and D) using the designed haptic device and two participants appeared the same mistake using Phantom Omni. It is worth noting that one participant made mistakes in two tests, and it may result from his poor ability of haptic perception. The accuracy rate of test 2 is 91 percent, showing that our haptic device has a ability to distinguish objects of different stiffness. In Experiment 2, all participants correctly detected the normal tissue and the abnormal tissue by using the two haptic devices.

In addition, a score for the four factors (Sensory, Realism, Comfort and Satisfaction) were obtained using a questionnaire. The QoE is the sum of four factors. The statistical results are shown in Fig. 11 and Table 6. In Table 6, we computed the average  $\bar{x}$  and standard deviation  $\sigma_x$  of each factor. In addition, we conducted a nonparametric test to analyze the statistical results. The QoE of our haptic device is not significantly different from that of Phantom Omni ( $QoE_{Our} = 15.09 \approx QoE_{Phantom} = 15.55$ , Mann-Whitney U test  $p = 0.1573 > 0.05$ , effect size is  $ES = 0.52$  and statistical power is  $power = 0.50$ ). Therefore, our device significantly enhances the quality of experience. The “Sensory” score of

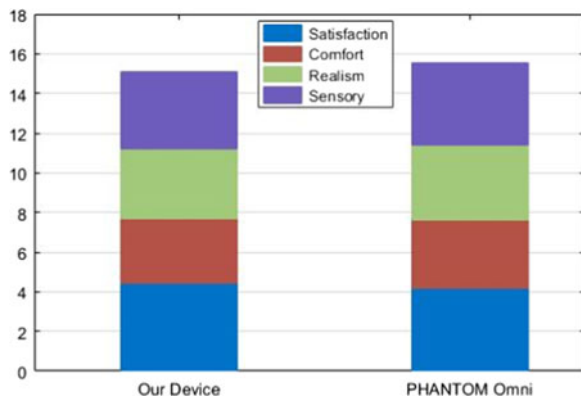


Fig. 11. Quality of experience. The QoE of our haptic device is not significantly different from that of Phantom Omni.

TABLE 6  
Means ( $\bar{x}$ ) and Standard Deviations ( $\sigma_x$ ) for Each Device with Respects to Each Factor

Factor	QoE	Sensory	Realism	Comfort	Satisfaction	
Our Device	15.09	4.45	3.23	3.50	3.91	$\bar{x}$
	0.9715	0.5096	0.5284	0.5118	0.2942	$\sigma_x$
Phantom Omni	15.55	4.19	3.45	3.73	4.18	$\bar{x}$
	0.8004	0.3948	0.5096	0.5505	0.3948	$\sigma_x$

our device is higher than that of Phantom Omni. Taking into account that the accuracy rate of distinguishing objects of different stiffness is identical using the two devices, the higher score of “Sensory” is possible due to the way of our device is closer to the natural manner.

## 5 DISCUSSION

The quantitative results show that the simulation data of the magnetic flux density used to generate force feedback is consistent with the experimental data. The presented self-adaptive fuzzy PID algorithm can control coil current accurately, which ensures precise haptic perception of the designed haptic device. The positioning performance of our stereoscopic tracking module was evaluated using the designed calibration platform. Although the location ball used in the experiment is bigger than the actual tip of our magnetic stylus, the position tracked by our stereoscopic tracking module is the actual position of the center of the location ball, which benefits from the design that red markers are embedded in the magnetic stylus. Moreover, our design can ensure that the tracking module tracks the same position in different trials for each location hole.

For the coil configuration of our haptic device, we have reasonably explained the design of the coil array compared to the existing methods [23], [26]. We describe interactive requirements using probability clouds and further present an algorithm to calculate the best coil attitude. The experimental results demonstrate its advantage of low power consumption, and it is easy to expand our haptic device to other applications such as entertainment industry. However, we just focus on two parameters of the coil configuration, that is the angle of each coil and the distance between coils, more coil parameters such as the number and the shape of coils should be concerned in future work.

The preliminary qualitative results demonstrate that our device can help users to distinguish objects of different stiffness and correctly detect tissue abnormality in the virtual environment. Therefore, the designed device has the potential for augmenting tissue stiffness perception in surgical simulation. The QoE of our haptic device is lower than that of Phantom Omni. However, the “Sensory” score of our device is higher. Our device does not require mechanical transmission and the magnetic stylus is flexible, thus the user can interact with virtual objects in a natural manner. Therefore, the higher “Sensory” score benefits from the question “Whether the interaction way is consistent with your habits of the real world”.

In this paper, tissue deformation model was built using the Vega software [44], which achieves real-time deformation simulation by reducing the dimension of the model.

However, the process of dimension reduction would affect the accuracy of the force feedback, which is one reason why the score of "Realism" factor is slightly lower in the questionnaire. In addition, we simulate tissue of different stiffness by setting different stiffness matrix for the objects and we obtained a tissue abnormality by embedding a lump into a normal tissue, which also affects the realistic of our model. To achieve realistic perception of tissue stiffness, a high precision simulation model needs to be studied for real-time haptic interaction.

## 6 CONCLUSION AND FUTURE WORK

We design a novel magnetic levitation haptic device for augmenting virtual tissue stiffness perception in this paper. Users can sense tissue in the virtual environment using the designed magnetic stylus in a natural manner. We present to calculate the best coil attitude and design an adjustable coil array, which provides a reasonable explanation of coil configuration compared with the existing methods. The calculated best coil attitude is beneficial for taking full advantage of the magnetic field. The quantitative experiments demonstrate advantages of high accuracy and low power consumption of the designed haptic device. In the qualitative experiments, the participants can accurately distinguish objects of different stiffness, as well as precisely detect the tissue abnormality using our haptic device.

To further improve the performance of our haptic device, we will investigate the visual-haptic interaction model with higher precision to achieve more accurate tissue stiffness perception. We also will integrate our device with the VR helmets, such as HTC Vive and Oculus Rift, to experience more immersive surgical scenarios.

## ACKNOWLEDGMENTS

We would like to thank Mingui Sun, Weixu Zhu and Guian Zhang for the insight discussion. The work is supported by the National Natural Science Foundation of China under Grant No. 61373107 and Wuhan Science and Technology Program under Grant No. 2016010101010022.

## REFERENCES

- [1] M. A. Otaduy, A. Okamura, and S. Subramanian, "Haptic technologies for direct touch in virtual reality," in *Proc. ACM SIGGRAPH 2016 Courses*, 2016, Art. no. 13.
- [2] A. Zenner and A. Krüger, "Shifty: A weight-shifting dynamic passive haptic proxy to enhance object perception in virtual reality," *IEEE Trans. Vis. Comput. Graph.*, vol. 23, no. 4, pp. 1285–1294, Apr. 2017.
- [3] T. R. Coles, D. Meglan, and N. W. John, "The role of haptics in medical training simulators: A survey of the state of the art," *IEEE Trans. Haptics*, vol. 4, no. 1, pp. 51–66, Jan.–Mar. 2011.
- [4] S. Ullrich and T. Kuhlen, "Haptic palpation for medical simulation in virtual environments," *IEEE Trans. Vis. Comput. Graph.*, vol. 18, no. 4, pp. 617–625, Apr. 2012.
- [5] G. De Gerssem, H. Van Brussel, and F. Tendick, "Reliable and enhanced stiffness perception in soft-tissue telemanipulation," *Int. J. Robot. Res.*, vol. 24, no. 10, pp. 805–822, 2005.
- [6] H. Liu, D. P. Noonan, K. Althoefer, and L. D. Seneviratne, "Rolling mechanical imaging: A novel approach for soft tissue modelling and identification during minimally invasive surgery," in *Proc. IEEE Int. Conf. Robot. Autom.*, 2008, pp. 845–850.
- [7] H. Liu, J. Li, X. Song, L. D. Seneviratne, and K. Althoefer, "Rolling indentation probe for tissue abnormality identification during minimally invasive surgery," *IEEE Trans. Robot.*, vol. 27, no. 3, pp. 450–460, Jun. 2011.
- [8] M. Li, H. Liu, J. Li, L. D. Seneviratne, and K. Althoefer, "Tissue stiffness simulation and abnormality localization using pseudo-haptic feedback," in *Proc. IEEE Int. Conf. Robot. Autom.*, 2012, pp. 5359–5364.
- [9] C. Neupert, S. Matich, N. Scherping, M. Kupnik, R. Werthschützky, and C. Hatzfeld, "Pseudo-haptic feedback in teleoperation," *IEEE Trans. Haptics*, vol. 9, no. 3, pp. 397–408, Jul.–Sep. 2016.
- [10] I. Nisky, F. Huang, A. Milstein, C. M. Pugh, F. A. Mussa-Ivaldi, and A. Karniel, "Perception of stiffness in laparoscopy—the fulcrum effect," *Stud. Health Technol. Informat.*, vol. 173, 2012, Art. no. 313.
- [11] H. I. Son, T. Bhattacharjee, and H. Hashimoto, "Effect of impedance-shaping on perception of soft tissues in macro-micro teleoperation," *IEEE Trans. Ind. Electron.*, vol. 59, no. 8, pp. 3273–3285, Aug. 2012.
- [12] D. Escobar-Castillejos, J. Noguez, L. Neri, A. Magana, and B. Benes, "A review of simulators with haptic devices for medical training," *J. Med. Syst.*, vol. 40, no. 4, pp. 1–22, 2016.
- [13] F. Arafsha, L. Zhang, H. Dong, and A. El Saddik, "Contactless haptic feedback: State of the art," in *Proc. IEEE Int. Symp. Haptic Audio Visual Environ. Games*, 2015, pp. 1–6.
- [14] R. Sodhi, I. Poupyrev, M. Glisson, and A. Israr, "AIREAL: Interactive tactile experiences in free air," *ACM Trans. Graph.*, vol. 32, no. 4, 2013, Art. no. 134.
- [15] T. Hoshi, "Development of aerial-input and aerial-tactile-feedback system," in *Proc. IEEE World Haptics Conf.*, 2011, pp. 569–573.
- [16] T. Carter, S. A. Seah, B. Long, B. Drinkwater, and S. Subramanian, "UltraHaptics: Multi-point mid-air haptic feedback for touch surfaces," in *Proc. 26th Annu. ACM Symp. User Interface Softw. Technol.*, 2013, pp. 505–514.
- [17] R. L. Hollis and S. E. Salcudean, "Lorentz levitation technology: A new approach to fine motion, robotics, teleoperation, haptic interfaces, and vibration isolation," in *Proc. 5th Int. Symp. Robot. Res.*, 1993, pp. 1–18.
- [18] R. Hollis, "Maglev haptics: Butterfly haptic's new user interface technology," in *Proc. ACM SIGGRAPH 2008 New Tech Demos*, 2008, Art. no. 23.
- [19] B. Wu, R. L. Klatzky, and R. L. Hollis, "Force, torque, and stiffness: Interactions in perceptual discrimination," *IEEE Trans. Haptics*, vol. 4, no. 3, pp. 221–228, Jul.–Sep. 2011.
- [20] P. Berkelman and M. Dzadovsky, "Extending the motion ranges of magnetic levitation for haptic interaction," in *Proc. 3rd Joint EuroHaptics Conf. Symp. Haptic Interfaces Virtual Environ. Teleoperator Syst.*, 2009, pp. 517–522.
- [21] P. J. Berkelman and M. Dzadovsky, "Large motion range magnet levitation using a planar array of coils," in *Proc. IEEE Int. Conf. Robot. Autom.*, 2009, pp. 1609–1610.
- [22] J. Hu, "Magnetic haptic feedback systems and methods for virtual reality environments," U.S. Patent App. 11/141,828, Jun. 1, 2005.
- [23] J. Hu, C. Chang, N. Tardella, J. Pratt, and J. English, "Effectiveness of haptic feedback in open surgery simulation and training systems," *Stud. Health Technol. Inf.*, vol. 119, pp. 213–218, 2006.
- [24] P. Berkelman, M. Miyasaka, and J. Anderson, "Co-located 3D graphic and haptic display using electromagnetic levitation," in *Proc. IEEE Haptics Symp.*, 2012, pp. 77–81.
- [25] P. Berkelman, S. Bozlee, and M. Miyasaka, "Interactive dynamic simulations with co-located maglev haptic and 3D graphic display," in *Proc. Int. Conf. Advances Comput.-Human Interactions*, 2013, pp. 324–329.
- [26] P. J. Berkelman and M. Dzadovsky, "Magnetic levitation over large translation and rotation ranges in all directions," *IEEE/ASME Trans. Mechatronics*, vol. 18, no. 1, pp. 44–52, Feb. 2013.
- [27] Q. Tong, Z. Yuan, M. Zheng, W. Zhu, G. Zhang, and X. Liao, "A novel magnetic levitation haptic device for augmentation of tissue stiffness perception," in *Proc. 22nd ACM Conf. Virtual Reality Softw. Technol.*, 2016, pp. 143–152.
- [28] A. M. Okamura, C. Basdogan, S. Baillie, and W. S. Harwin, "Haptics in medicine and clinical skill acquisition [special section intro.]," *IEEE Trans. Haptics*, vol. 4, no. 3, pp. 153–154, Jul.–Sep. 2011.
- [29] G. Stetten, et al., "Hand-held force magnifier for surgical instruments," in *Proc. Int. Conf. Inf. Process. Comput.-Assisted Interventions*, 2011, pp. 90–100.
- [30] T. Hoshi, D. Abe, and H. Shinoda, "Adding tactile reaction to hologram," in *Proc. 18th IEEE Int. Symp. Robot Human Interactive Commun.*, 2009, pp. 7–11.
- [31] B. Long, S. A. Seah, T. Carter, and S. Subramanian, "Rendering volumetric haptic shapes in mid-air using ultrasound," *ACM Trans. Graph.*, vol. 33, no. 6, 2014, Art. no. 181.

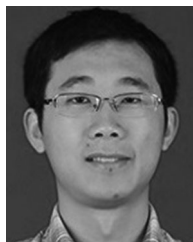
- [32] S. B. Kesner and R. D. Howe, "Discriminating tissue stiffness with a haptic catheter: Feeling the inside of the beating heart," in *Proc. IEEE World Haptics Conf.*, 2011, pp. 13–18.
- [33] Z. F. Quek, S. B. Schorr, I. Nisky, A. M. Okamura, and W. R. Provancher, "Augmentation of stiffness perception with a 1-degree-of-freedom skin stretch device," *IEEE Trans. Human-Mach. Syst.*, vol. 44, no. 6, pp. 731–742, Dec. 2014.
- [34] M. Li, et al., "A novel tumor localization method using haptic palpation based on soft tissue probing data," in *Proc. IEEE Int. Conf. Robot. Autom.*, 2014, pp. 4188–4193.
- [35] R. L. Hollis, S. E. Salcudean, and A. P. Allan, "A six-degree-of-freedom magnetically levitated variable compliance fine-motion wrist: Design, modeling, and control," *IEEE Trans. Robot. Autom.*, vol. 7, no. 3, pp. 320–332, Jun. 1991.
- [36] P. J. Berkelman and R. L. Hollis, "Lorentz magnetic levitation for haptic interaction: Device design, performance, and integration with physical simulations," *Int. J. Robot. Res.*, vol. 19, no. 7, pp. 644–667, 2000.
- [37] R. L. Hollis, "Butterfly haptics: A high-tech startup [entrepreneur]," *IEEE Robot. Autom. Mag.*, vol. 17, no. 4, pp. 14–17, Dec. 2010.
- [38] R. L. Hollis, "Magnetic levitation haptic interface system," U.S. Patent 8 497 767, Jul. 30, 2013.
- [39] P. Berkelman and R. L. Hollis, "Dynamic performance of a magnetic levitation haptic device," in *Proc. Intell. Syst. Adv. Manuf.*, 1997, pp. 140–149.
- [40] P. Berkelman, "A novel coil configuration to extend the motion range of lorentz force magnetic levitation devices for haptic interaction," in *Proc. IEEE/RSJ Int. Conf. Intell. Robots Syst.*, 2007, pp. 2107–2112.
- [41] P. Berkelman and M. Dzadovsky, "Magnet levitation and trajectory following motion control using a planar array of cylindrical coils," in *Proc. ASME Dyn. Syst. Control Conf.*, 2008, pp. 923–930.
- [42] Z. Zhang, "A flexible new technique for camera calibration," *IEEE Trans. Pattern Anal. Mach. Intell.*, vol. 22, no. 11, pp. 1330–1334, Nov. 2000.
- [43] M. Pedersoli, J. González, A. D. Bagdanov, and J. J. Villanueva, "Recursive coarse-to-fine localization for fast object detection," in *Proc. Eur. Conf. Comput. Vis.*, 2010, pp. 280–293.
- [44] F. S. Sin, D. Schroeder, and J. Barbič, "Vega: Non-linear FEM deformable object simulator," *Comput. Graph. Forum*, vol. 32, no. 1, pp. 36–48, 2013.
- [45] K. Killki, "Quality of experience in communications ecosystem," *J. Universal Comput. Sci.*, vol. 14, no. 5, pp. 615–624, 2008.
- [46] F. Danieau, et al., "Framework for enhancing video viewing experience with haptic effects of motion," in *Proc. IEEE Haptics Symp.*, 2012, pp. 541–546.
- [47] F. Danieau, J. Fleureau, P. Guillotel, N. Mollet, A. Lécuyer, and M. Christie, "HapSeat: Producing motion sensation with multiple force-feedback devices embedded in a seat," in *Proc. 18th ACM Symp. Virtual Reality Softw. Technol.*, 2012, pp. 69–76.



**Qianqian Tong** is working toward the PhD degree in the School of Computer, Wuhan University. Her research interests include human-computer interaction, computer vision, machine learning, and medical imaging.



**Zhiyong Yuan** is a professor in the School of Computer, Wuhan University. His research interests include virtual reality, human-computer interaction, machine learning, embedded system, virtual surgery, and medical imaging.



**Xiangyun Liao** is an assistant professor in the Shenzhen Institute of Advanced Technology, Chinese Academy of Sciences. His research interests include virtual reality, physics based modeling, and medical imaging.



**Mianlun Zheng** is working toward the master's degree in the School of Computer, Wuhan University. Her research interests include virtual reality and physics based modeling.



**Tianchen Yuan** is working toward the master's degree in the School of Computer, Wuhan University. His research interests include human-computer interaction, computer vision, and machine learning.



**Jianhui Zhao** is an associate professor in the School of Computer, Wuhan University. His research interests include computer graphics, image processing, and pattern recognition.

▷ For more information on this or any other computing topic, please visit our Digital Library at [www.computer.org/publications/dlib](http://www.computer.org/publications/dlib).